

Photonic Topological Insulators: A Beginner's Introduction

Dia'aaldin J. Bisharat, Robert J. Davis, Yun Zhou, Prabhakar R. Bandaru, and Daniel F. Sievenpiper

The control and manipulation of electromagnetic (EM) waves has reached a new level with the recent understanding of topological states of matter. These metamaterials have the potential to revolutionize many areas in traditional EM design, from highly robust cavities to small-footprint waveguides. Much of the past literature has been on the cutting edge of condensed-matter physics, but there are now ample opportunities to explore their usage for practical microwave and optical devices.

To assist the beginner, in this tutorial, we give a basic introduction to the essential concepts of topological phenomena in EM systems, including geometric phases, topological invariants, pseudospin states, and the integer/valley/spin quantum Hall effects (QHEs). Our focus is on engineered photonic topological insulators (PTIs) in 2D systems. We highlight methods for characterizing such structures and how they result in unique waveguiding properties. In addition, we provide recipes on how to realize PTIs using photonic crystals (PhCs) and metasurfaces, examine differences among different types of PTIs, and discuss the limitations and advantages of some of the existing enabling platforms.

Digital Object Identifier 10.1109/MAP.2021.3069276
Date of current version: 2 June 2021

EDITOR'S NOTE

"Everything should be made as simple as possible," said Einstein. Unfortunately, today's scientific knowledge is often presented in an obscure fashion, and the maelstrom of unfiltered information assailing us daily does not favor clarity. Electromagnetics is no exception to this trend. Luckily, a platform such as *IEEE Antennas and Propagation Magazine* represents a fantastic opportunity to disseminate knowledge via paths that deviate from common routes and, hence, to provide alternative explanations that may demystify previously inaccessible concepts. The "Electromagnetic Perspectives" column aims to leverage this opportunity with articles that include the following features:



Christophe Caloz

- historical contextualization
- maximal simplification (without compromising accuracy)
- pedagogical creativity
- first-principles methodology.

Authors feeling that they may provide a contribution in the spirit of this column are welcome to contact me at christophe.caloz@polymtl.ca.

Topology (from the Greek τόπος, meaning "place or location," and λόγος, signifying "study") is a field of mathematics that deals with geometrical properties and spatial relations that are preserved under continuous deformations. It has many ramifications in science and engineering, one of them being topological insulators. Topological insulators were first reported as a quantum mechanical effect in electronics, but it has been recently transposed to photonics, where it has become a very popular topic. This article by Bisharat et al. offers an introduction and a broad picture of the field that, I hope, are of great interest to the readers of the magazine.

INTRODUCTION

In much the same way as PhCs applied the ideas of solid-state physics to photons [1], i.e., EM waves, the new field of PTIs [2] finds its origins in the world

of electronic systems. In electronic TIs, electrons propagate along certain directions only on the exterior of the system. This explains part of the name: it is an "insulator" inasmuch as it acts

like a regular electrical insulator within the bulk of a material. “Topological,” on the other hand, comes from the global topology of the energy band structure since it can be categorized by an integer (the “topological invariant”) that does not depend on the fine details of the system (see Figure 1). The occurrence of electrical current on the surface of TIs—and how it responds to changes in energy—is credited to this topological invariant (see Figure 2) rather than minor changes to the surface, as in ordinary materials.

TIs found their start in the 1980s with the discovery of the QHE in a 2D electron gas when subjected to periodic potentials and external magnetic fields [3], [4]. As in the normal Hall effect, applying a magnetic field causes the electrons to spin in cyclotron orbits, with their frequencies being determined by the strength of the B field. When the material is strongly confined to 2D and cooled to very low temperatures, the quantization of the energy of these orbits becomes relevant, with the difference between the allowed energies becoming very large as the field strength increases. When the strength of the B field varies enough to permit or remove an energy level, there will be a sudden jump in the transverse conductivity by an exact multiple of the fundamental constants.

Hence, the QHE shows that conductivity is fundamentally discrete [5]. Importantly, it was found [6] that this discrete behavior could be explained by a special phase (called the *geometric* or *Berry phase*, detailed in the “Geometric Phase” section) that each electron accumulates as it orbits in cyclotron motion in reciprocal (k) space.

How does topology relate to this? As it turns out, the discrete nature of the conductance is highly robust to deformations to the bulk of the material, and it can be shown that the added geometric phase responsible for the quantization is tied directly to the mathematical framework of topological invariants (see Figure 2) [3], [6], [7]. This has some important consequences: it gives us a simple means to classify materials (i.e., bandgap materials) by calculating their topological invariant (which is a property of the bulk material), and it results in

the technologically useful effects that TIs offer.

Materials that have an invariant of zero are “trivial,” and they act the same as ordinary materials. If the invariant is nonzero, however, then the effects of the geometric phase become relevant, and “nontrivial” effects can be observed. One of the most startling effects is what happens at the edge between a nontrivial material and a trivial material (or another nontrivial material with a different invariant), where a highly robust transport mode can exist [5].

These special modes, called *edge modes*, exist within the bandgap of the nontrivial material, and they can be explained by the sudden change in the invariant across the boundary (e.g., going from one to zero). Even more remarkable is that electrons moving along these boundaries must do so in one direction only, with no possibility of scattering back in the other direction (illustrated in

Figure 1) [8]. These edge modes are the corollary of the quantization of conductivity in the QHE.

In repeated experiments, these edge states are observed regardless of the impurities in different material samples [9]. Since the invariant is resistant to a wide range of distortions to the material, the edge states are said to be topologically “protected”—i.e., guaranteed to exist so long as the invariant stays the same [5]. This is of technological importance due to the potential to reduce power consumption by eliminating sources of loss as well as simplify manufacturing by increasing defect tolerances. These discoveries led to the Nobel Prize in Physics being awarded to Thouless, Haldane, and Kosterlitz in 2016.

These systems with topological behavior are a consequence of the wave nature of the electrons, not specifically their quantum interactions [10]. As a result, it is possible to construct classical

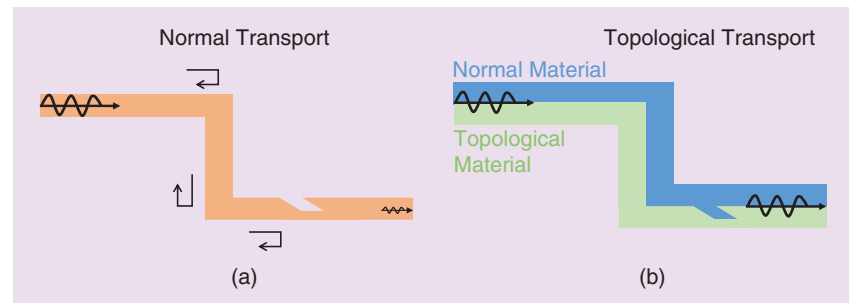


FIGURE 1. (a) Normal versus (b) topologically protected transport. The normal case has backscatter at sharp corners and defects, whereas the topological one does not.

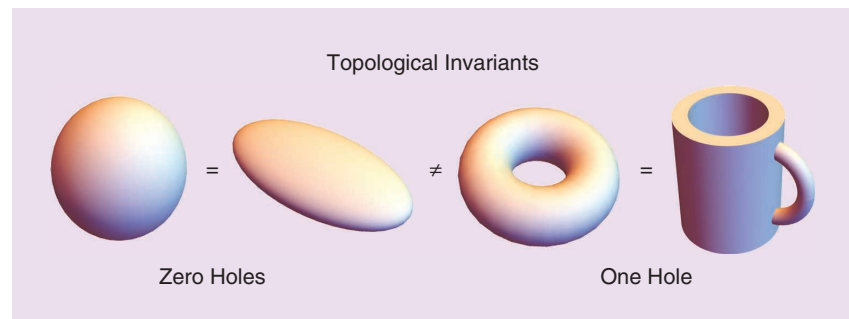


FIGURE 2. Topology concerns quantities that are preserved under continuous deformations of objects. A transformation is “continuous” if it does not cause any sharp cuts or tears in the object. The number of holes in a closed surface is an example of a topological invariant since a hole cannot be added or removed continuously: a torus can be stretched and pulled into a coffee cup shape, but not a sphere. Electrical conductance in TIs is also determined by a topological invariant, called the *Chern number* (C), where the object is an energy band in the Brillouin zone, and the “holes” are determined by the accumulation of the Berry phase.

wave systems with analogous properties to their electronic counterparts. This opens the door to a vast range of theoretical proposals and experimental demonstrations. Replacing the electron with a photon (along with a reinterpretation of some quantities), we arrive at PTIs, which demonstrate many of the same features of TIs [2] and are the primary subject of this tutorial (see “Side Note 1”).

SIDE NOTE 1

Although the field of PTIs originated from the electronic version, there are some fundamental differences between the two. The most significant is that photons are bosons, whereas electrons are fermions. This difference manifests itself in the ways that different symmetries (like time reversal, written as an operator T) can change how a system behaves.

Specifically, time reversal for fermions has the relationship $T^2 = -1$, whereas for bosons, it is $T^2 = +1$. A more practical concern is that absorption in the medium can be an issue in photonics. Nevertheless, many of the most technologically relevant features of TIs (including backscatter immunity) can still be found in photonic systems, so long as care is taken to distinguish the circumstances in which they can exist.

In this tutorial, we outline the basic concept of the geometric phase and extend it to periodic systems in which topological properties emerge. We focus on 2D PhCs and showcase the physical implications of Chern numbers and topological transitions that can arise in such systems. In addition, we discuss the formation of degeneracy (Dirac) points in PhCs and then the various mechanisms to introduce topological phases that make different types of PTIs. Finally, we discuss recent developments in and future perspectives on this emerging field.

GEOMETRIC PHASE

The key idea behind topological effects in all areas is the geometric phase, a universal concept that emerges when a parameter describing a system is gradually varied in a closed cycle [11]. This phase was first proposed in 1956 by Pancharatnam for the propagation of light through a sequence of polarizers [12] and was later generalized by Berry for quantum mechanics [13]. Many phenomena in physics can be attributed to the geometric phase, from the mechanical Foucault pendulums [14] to the polarization in helical waveguides [15].

Any wave possesses an amplitude (call it E_0) and an ordinary phase (ϕ) at a given position and time, $E(\mathbf{r}, t) = E_0(\mathbf{r})e^{j\phi t}$. When the values of \mathbf{r} and t are slowly changed from \mathbf{r}_0 and t_0 to distinct intermediate values \mathbf{r}_1

and t_1 , then smoothly changed back to \mathbf{r}_0 and t_0 , we would intuitively expect that the initial value of $E(\mathbf{r}, t)$ would be exactly the same as the final value. However, there are some physically important cases where this intuition fails, as in the case shown in Figure 3.

If we take a tangent vector (the red arrows) and slide it along a path on a sphere (the black arrows), returning it to the starting position, it will no longer be pointing in the same direction. Hence, the starting value no longer matches the final value. Upon its return to the north pole, the orientation of the vector is rotated by an angle ϕ , which, in this situation, is equal to $\pi/2$. Note that this is the case only because the path is a closed loop: if the tangent retraced the same path to return to the start (enclosing no area), the orientations would match, and ϕ would be zero. In the closed-path case, we can consider the angle to be an added phase, the geometric phase, that causes the initial and final values to differ. This phase is geometric because it corresponds to a geometric area (Ω , shaded in blue) of the parameter space that the path encloses.

If we think of the sphere in Figure 3(a) as the sphere of constant wave vector \mathbf{k} and the vector as the electric field (E-field), this parallel transport explains the change in polarization in the helical and bent waveguides [Figure 3(b)] [16]. In the example of a bent waveguide, if polarized light gradually changes direction from z to $-x$, then from $-x$ to y , and finally back to z , the wave will pick up a geometric phase that is added to the complex exponential form of the E-field. The “path,” in this case, is the path traced over the \mathbf{k} sphere as the wave vector, corresponding to the direction, is changed. In this situation, the extra phase (in the form of the polarization direction) can be attributed to the E-field always being perpendicular to the direction of propagation; therefore, as the direction of propagation is changed, the polarization must necessarily be altered, despite the propagation direction eventually returning to the starting value. Note that this effect is possible only due to the existence of

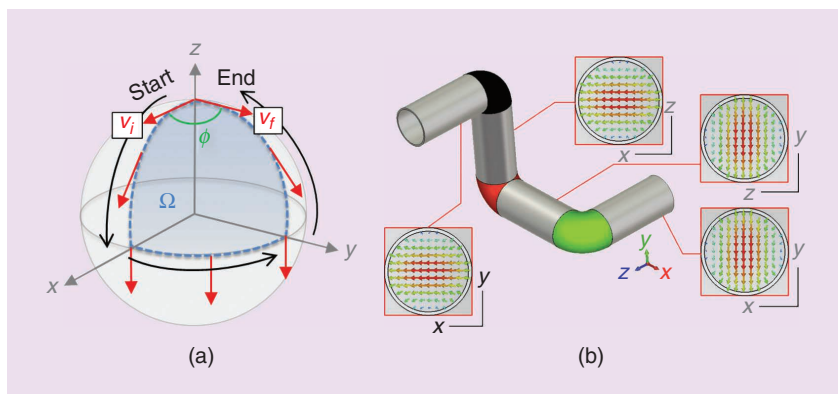


FIGURE 3. (a) The geometric phase from parallel transport. (b) The polarization (shown as the vector E-field inset at different locations) in a bent circular waveguide shows that, as the propagation path is varied and then returned to its initial state, there can be a phase shift to the polarization state, which is due to the geometric phase. (Source: [16]).

two degenerate modes in the waveguide (from the circular symmetry).

BERRY PHASE, CONNECTION, AND CURVATURE

A geometric phase can emerge due to the gradual variation of a state in many types of parameter spaces, including the momentum space of a periodic system, like those of a PhC [17]. For any path that traverses an allowed band of a periodic system and does not intersect with any other band, the wave vector \mathbf{k} (Bloch momentum) varies in closed loops due to the lattice periodicity, where $\mathbf{k}_{-\pi} \equiv \mathbf{k}_\pi$. In a 2D crystal, \mathbf{k} traverses the surface of a torus geometry, which bounds the entire Brillouin zone (BZ) (see Figure 4). Many of the most important topological properties appear in such systems and are a simple platform to understand how they emerge.

The literature on TIs employs a great deal of terminology, most of which merely refers to a few mathematical constructions that assist in characterizing when a topological invariant is nontrivial. Fortunately, most of these constructions have parallels to standard EM theory and provide straightforward methods to numerically calculate topological features of real systems.

Consider a lattice described by a general eigenvalue problem in momentum space:

$$H(\mathbf{k}) \cdot \psi_n(\mathbf{k}) = \lambda_n(\mathbf{k}) \psi_n(\mathbf{k}), \quad (1)$$

where $\lambda_n(\mathbf{k})$ is the eigen energy, and $\psi_n(\mathbf{k})$ is the normalized eigen wave function of $H(\mathbf{k})$ (often called the *Hamiltonian* in the literature) at each \mathbf{k} for the n th band, which can be determined via Bloch's theorem. In the following, we will make use of the shorthand notation of the inner product,

$$\langle \mathbf{A}(\mathbf{r}) | \mathbf{B}(\mathbf{r}) \rangle \equiv \int \mathbf{A}(\mathbf{r})^\dagger \cdot \mathbf{B}(\mathbf{r}) d\mathbf{r}, \quad (2)$$

to refer to the integration of two vector functions \mathbf{A} and \mathbf{B} over a variable \mathbf{r} , with \dagger denoting Hermitian conjugation. Hence, *normalized*, in this case, means $\langle \psi_n(\mathbf{k}) | \psi_n(\mathbf{k}) \rangle = 1$. Gradually changing the \mathbf{k} along a given energy band causes a phase accumulation

associated with the slow evolution of $\psi_n(\mathbf{k})$. Under most circumstances, when \mathbf{k} returns back to where it started, this accumulation results in zero total phase, but, like in the examples of the "Geometric Phase" section, special cases can arise where a nonzero geometric phase is added. In the PTI literature, the geometric phase is referred to by the name *Berry phase*, specifically to recall Berry's formulation in quantum mechanics [13].

To calculate the total Berry phase, we need a means to add up the phase contributions from each small change to the wave function. The phase shift between two ψ_n states infinitesimally separated by $\Delta\mathbf{k}$ can be represented by their inner product [16], expanded as a low-order Taylor series as

$$\begin{aligned} \langle \psi_n(\mathbf{k}) | \psi_n(\mathbf{k} + \Delta\mathbf{k}) \rangle & \approx 1 + \Delta\mathbf{k} \langle \psi_n(\mathbf{k}) | \nabla_{\mathbf{k}} | \psi_n(\mathbf{k}) \rangle \\ & = \exp[-i\Delta\mathbf{k} \cdot \mathbf{A}_n(\mathbf{k})]. \end{aligned} \quad (3)$$

Here, we can see that $\Delta\mathbf{k} \cdot \mathbf{A}_n(\mathbf{k})$ is the phase shift over $\Delta\mathbf{k}$, and $\mathbf{A}_n(\mathbf{k})$ is the rate of change of the phase shift (see "Side Note 2"). $\mathbf{A}_n(\mathbf{k})$ is called the *Berry connection* or *Berry vector potential*:

$$\mathbf{A}_n(\mathbf{k}) = i \langle \psi_n(\mathbf{k}) | \nabla_{\mathbf{k}} | \psi_n(\mathbf{k}) \rangle. \quad (4)$$

Therefore, the Berry phase for the n th band is defined as the integral of $\mathbf{A}_n(\mathbf{k})$ over some closed path l in the \mathbf{k} space:

$$\phi_n = \oint_l d\mathbf{k} \cdot \mathbf{A}_n(\mathbf{k}). \quad (5)$$

The path l is simply a smooth curve of values over the BZ, such as the blue and red lines shown in Figure 4(b). If we know what a given wave function looks like in the BZ, we could use (5) to calculate the Berry phase for that path. However, there is a catch: the Berry connection $\mathbf{A}_n(\mathbf{k})$ is not uniquely defined. If a phase change $\zeta(\mathbf{k})$ is added to the eigen wave function $\psi_n(\mathbf{k})$, where $\zeta(\mathbf{k})$ is a periodic function with $\zeta(\mathbf{k}_{\text{end}}) = \zeta(\mathbf{k}_{\text{begin}}) + 2m\pi$, the new wave function $e^{i\zeta(\mathbf{k})} \psi_n(\mathbf{k})$ is still an eigen wave function to $H(\mathbf{k})$. The Berry connection is then transformed as

$\mathbf{A}_n(\mathbf{k}) \rightarrow \mathbf{A}_n(\mathbf{k}) - (\partial/\partial\mathbf{k})\zeta(\mathbf{k})$, where it changes its formula with a different choice of $\zeta(\mathbf{k})$.

The Berry phase, on the other hand, is invariant modulo 2π :

$$\begin{aligned} \oint_l d\mathbf{k} \cdot \mathbf{A}_n(\mathbf{k}) & \rightarrow \oint_l d\mathbf{k} \cdot \mathbf{A}_n(\mathbf{k}) \\ & - \oint_l \frac{\partial}{\partial\mathbf{k}} \zeta(\mathbf{k}) d\mathbf{k} \rightarrow \oint_l d\mathbf{k} \cdot \mathbf{A}_n(\mathbf{k}) - 2m\pi. \end{aligned} \quad (6)$$

This can also be understood qualitatively. As the wave vector \mathbf{k} slowly travels around the loop of a band, the wave function $\psi_n(\mathbf{k})$ eventually returns to where it starts and picks up a phase of a multiple of 2π , with most systems picking up zero [11]. Since the Berry connection depends on how we set up the calculation, yet we know that the Berry phase should not, it is helpful (especially for numerical

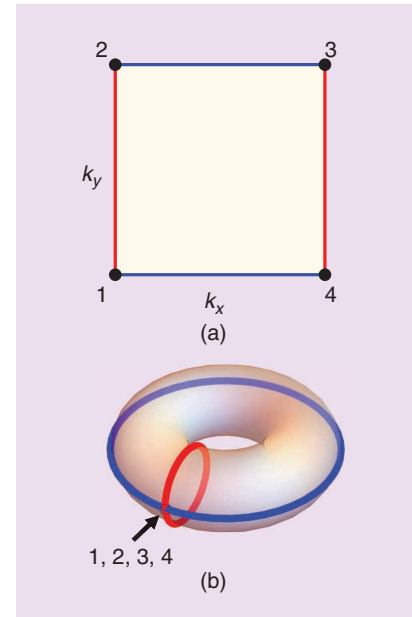


FIGURE 4. The (a) BZ can be considered as a (b) torus by taking each periodic boundary (red and blue) and connecting them together.

SIDE NOTE 2

The notation $\langle \alpha | \beta \rangle$ represents the inner product of the wave functions α and β , whereas $\langle \alpha | \nabla_{\mathbf{k}} | \beta \rangle$ denotes the inner product of α and $\nabla_{\mathbf{k}}\beta$.

purposes) to define a quantity that will be invariant to any arbitrary phase $\zeta(\mathbf{k})$ that we may add.

The Berry curvature, or Berry flux, a quantity that is invariant under such transformation, can be constructed by taking the curl of the Berry connection:

$$\mathbf{\Omega}_n(\mathbf{k}) = \nabla_{\mathbf{k}} \mathbf{A}_n(\mathbf{k}). \quad (7)$$

Then, using Stokes's theorem, the Berry phase can be rewritten as the integral of the Berry curvature:

$$\phi_n = \int_S d^2\mathbf{k} \cdot \mathbf{\Omega}_n(\mathbf{k}), \quad (8)$$

where the integration is over the surface bounded by the path l [16].

SIDE NOTE 3

Why is the Chern number always an integer? A simple explanation comes from comparing the equations with those of the magnetic field. The Berry curvature has the same form as the magnetic field, where the Berry connection takes the place of the magnetic vector potential (hence, the term *Berry vector potential*; likewise, the Berry phase can be thought of as a magnetic flux):

$$\mathbf{\Omega}_n = \nabla_{\mathbf{k}} \times \mathbf{A}_n \Leftrightarrow \mathbf{B} = \nabla_{\mathbf{r}} \times \mathbf{A}. \quad (S1)$$

Since the Chern number is just the integral of the Berry curvature, this is the \mathbf{k} -space version of integrating the magnetic field:

$$C_n = \int \mathbf{\Omega}_n \cdot d\mathbf{k} \Leftrightarrow \int \mathbf{B} \cdot d\mathbf{r}. \quad (S2)$$

From Gauss' law for \mathbf{B} fields, we know that doing so will always give zero, unless there exists a magnetic monopole in the integration area. In such a case, the integral will give an integer multiple of monopole charges. In contrast to the \mathbf{B} field, the Berry phase can contribute "monopoles" to the Berry curvature, the number of which is the Chern number [16]. Hence, the Chern number must be an integer. Further proofs can be found in [2] and [7].

TOPOLOGY IN 2D PhCs

The previous section dealt with the general concepts of the geometric phase in periodic media, regardless of the physical setting (i.e., electronic, photonic, and so on). To make this explicit, here, we show how this theory can be specialized for 2D EM systems. For EM waves, the eigenvalue problem space is described by the macroscopic Maxwell equations. For nonbianisotropic materials in 2D, the magnetic field can be eliminated—for simplicity, when treating transverse magnetic (TM) modes, given by the E_z -field alone—and Maxwell's equations can be recast in a compact form as

$$\nabla_{\mathbf{r}} [\boldsymbol{\mu}^{-1}(\mathbf{r}) \nabla_{\mathbf{r}} E_z(\mathbf{r})] = \omega^2 \boldsymbol{\epsilon}(\mathbf{r}) E_z(\mathbf{r}), \quad (9)$$

where ω is the angular frequency; $E_z(\mathbf{r})$ is the z component of the E-field (hereafter, we will drop the z subscript); and $\boldsymbol{\mu}(\mathbf{r})$ and $\boldsymbol{\epsilon}(\mathbf{r})$ are the magnetic permeability and dielectric permittivity tensors, respectively. Note that we are ignoring dispersive effects for now, but further analysis shows this is valid in many cases [16]. By applying Bloch's theorem to (9), the eigen wave function can be obtained in the form of eigen E-field $E_{n,\mathbf{k}}(\mathbf{r})$, assuming a periodicity of the material parameters [1].

Since the eigenvalue problem involves the dielectric permittivity $\boldsymbol{\epsilon}(\mathbf{r})$ on the right-hand side of (9), the inner product of two eigen wave functions $E_{n,\mathbf{k}_1}(\mathbf{r})$ and $E_{n,\mathbf{k}_2}(\mathbf{r})$ can be written as

$$\begin{aligned} \langle E_{n,\mathbf{k}_1}(\mathbf{r}) | E_{n,\mathbf{k}_2}(\mathbf{r}) \rangle \\ = \int d^2\mathbf{r} E_{n,\mathbf{k}_1}^*(\mathbf{r}) \boldsymbol{\epsilon}(\mathbf{r}) E_{n,\mathbf{k}_2}(\mathbf{r}), \end{aligned} \quad (10)$$

where $*$ denotes complex conjugation. The Berry connection then takes the form of

$$\begin{aligned} \mathbf{A}_n(\mathbf{k}) &= i \langle E_{n,\mathbf{k}} | \nabla_{\mathbf{k}} | E_{n,\mathbf{k}} \rangle \\ &= i \int d^2\mathbf{r} E_{n,\mathbf{k}}^*(\mathbf{r}) \boldsymbol{\epsilon}(\mathbf{r}) \nabla_{\mathbf{k}} E_{n,\mathbf{k}}(\mathbf{r}). \end{aligned} \quad (11)$$

As in the general case, $E_{n,\mathbf{k}}$ is normalized such that $\langle E_{n,\mathbf{k}} | E_{n,\mathbf{k}} \rangle = 1$. Subsequently, the Berry curvature and phase can be written as discussed earlier.

CHERN NUMBER

With the aid of the Berry curvature, we can calculate the Berry phase that a given EM mode may acquire for a 2D PhC lattice. As mentioned in the "Introduction" section, the relationship to topology comes in the form of an invariant tying a nonzero Berry phase to the edge modes. For EM systems, this invariant is called the *Chern number*, after Chinese American mathematician Shiing-Shen Chern.

The Chern number always takes an integer value (see "Side Note 3"). When it is nonzero, the 2D photonic system is said to be topologically nontrivial. The Chern number of the n th band of a 2D lattice is simply the Berry phase over the full BZ:

$$C_n = \frac{1}{2\pi} \int_{\text{BZ}} d^2\mathbf{k} \Omega_n(k_x, k_y), \quad (12)$$

where, in 2D, the Berry curvature only has two terms:

$$\Omega_n(k_x, k_y) = \frac{\partial A_{k_y}^n}{\partial k_x} - \frac{\partial A_{k_x}^n}{\partial k_y}, \quad (13)$$

where A^n is the Berry connection for the n th mode:

$$A_{k_x}^n = i \int d^2\mathbf{r} E_{n,\mathbf{k}}^*(\mathbf{r}) \boldsymbol{\epsilon}(\mathbf{r}) \frac{\partial E_{n,\mathbf{k}}(\mathbf{r})}{\partial k_x}, \quad (14)$$

$$A_{k_y}^n = i \int d^2\mathbf{r} E_{n,\mathbf{k}}^*(\mathbf{r}) \boldsymbol{\epsilon}(\mathbf{r}) \frac{\partial E_{n,\mathbf{k}}(\mathbf{r})}{\partial k_y}. \quad (15)$$

When calculated for an arbitrary polarized band over the whole BZ, the Chern number, expressed by C_n , takes a nonzero value only when the time-reversal symmetry (TRS) is broken for the lattice [2]. The most common case when this happens is if a magnetic field is applied (the Faraday and Kerr effects). In such cases, the system is often called a *Chern insulator* or *Chern PTI*.

However, there are a few ways to observe topological effects, even when the TRS is retained [4]. Such systems are still reciprocal (i.e., they cannot form true isolators), but they can display immunity to certain types of backscatter and act as robust polarization filters [18].

One popular version of time-reversal-symmetric PTIs is the "valley" PTI,

which associates different directions (Γ to K and Γ' to K') in \mathbf{k} space with “valley Chern numbers.” To calculate the valley Chern number C_v , the integral in (12) is simply performed over only one half of the BZ, such that two ordinarily identical high-symmetry points (K and K') are separated. This gives two different values of C_v , one for each half of the BZ. Added together, they will equal the normal Chern number (zero for reciprocal systems), but, considered separately, they can be nonzero under special cases [19].

The other major reciprocal PTI is the “spin” PTI, which associates the handedness of a circularly polarized mode (or other combinations of modes) with a “spin Chern number” C_s [20]. In general, these spins/polarizations are constructed by a superposition of two or more eigen fields from multiple bands at the same frequency (see “Side Note 4”). Each polarization (right- and left-handed) corresponds to its own value of C_s [20], [21]. As such, the E-field in the inner product definition must be replaced with the field associated with a given polarization.

NUMERICAL CALCULATION OF THE CHERN NUMBER

In calculations of the Chern number for simulations or experiments, we need to discretize the continuous 2D BZ into a lattice, as shown in Figure 5. The shown discretization is for a square BZ (for square lattices), but the same methods will work on triangular lattices, where the usual hexagonal BZ is shifted to form a rhombus [23], [24]. The Chern number can be written as [23], [24]

$$C_n = \frac{1}{2\pi} \sum_{k_x, k_y} \Omega_n(k_x, k_y) \Delta k_x \Delta k_y, \quad (16)$$

where

$$\begin{aligned} \Omega_n(k_x, k_y) \Delta k_x \Delta k_y &= (A_{k_y}^n(k_x + \Delta k_x, k_y) - A_{k_y}^n(k_x, k_y)) \Delta k_y \\ &\quad - (A_{k_x}^n(k_x, k_y + \Delta k_y) - A_{k_x}^n(k_x, k_y)) \Delta k_x. \end{aligned} \quad (17)$$

Since Δk_x is small,

$$\begin{aligned} A_{k_x}^n(k_x, k_y) \Delta k_x &\approx i \ln \langle E_n(k_x, k_y) | E_n(k_x + \Delta k_x, k_y) \rangle. \end{aligned} \quad (18)$$

SIDE NOTE 4

There are several ways of defining a spin Chern number. The different formulations depend on how the spins are rigorously related to a true topological invariant of the physical system. In general, the invariant of a spin PTI is frequently referred to as a Z_2 topological invariant [22], distinct from the ordinary Chern number, but, in this tutorial, it sufficient to consider it as a subtype of the standard Chern number C_n , albeit specialized to a given spin definition.

If we number the four vertices of a small cell as 1, 2, 3, and 4 in a clockwise direction, as shown in Figure 5, the integral of the Berry curvature over the grid can then be written as

$$\begin{aligned} \Omega_n(k_x, k_y) \Delta k &= -i (\ln \langle E_{n,1} | E_{n,2} \rangle \\ &\quad + \ln \langle E_{n,2} | E_{n,3} \rangle + \ln \langle E_{n,3} | E_{n,4} \rangle \\ &\quad + \ln \langle E_{n,4} | E_{n,1} \rangle) \\ &= -i \ln (\langle E_{n,1} | E_{n,2} \rangle \langle E_{n,2} | E_{n,3} \rangle \\ &\quad \langle E_{n,3} | E_{n,4} \rangle \langle E_{n,4} | E_{n,1} \rangle). \end{aligned} \quad (19)$$

Here,

$$\langle E_{n,p} | E_{n,q} \rangle = \sum_{w,m} E_{n,p}^*(w, m) \epsilon(w, m) E_{n,q}(w, m) \Delta s, \quad (20)$$

where $p, q = \{1, 2, 3, 4\}$ denotes the four vertices; (w, m) indicates the (w, m) th discretized cell in the real space;

$\Delta k = \Delta k_x \Delta k_y$; and Δs is the area of the discretized lattice in the real space. Equation (19) shows that the integral of the Berry curvature over each small cell in the BZ can be obtained by taking the inner products of the eigen E-fields at adjacent vertices in a clockwise order, as illustrated by the inset in Figure 5.

Substituting (19) into the summation in (16), we get a discrete approximation of the Chern number. It can be shown that this approximation converges to the (continuous variable) Chern number at the limit $\Delta k_{x(y)} \rightarrow 0$ [25]. Fortunately, it also rapidly converges, often as coarse a grid, as 24×24 cells enough for accurate determination of the Chern number [23], [25].

The spin Chern number can be computed by separating the two distinct spin eigenmodes (generally polarization based) and performing the Chern number calculation on each [20]. For non-trivial spin PTIs, this will result in two identical values, each being the negative of the other [22], [23]. For valley Chern number calculations, only half of the BZ is integrated in (20) to account for the contribution of a finite region in the momentum space that corresponds to specific high-symmetry points in the BZ [23] (see “Side Note 5”).

From a practical perspective, the Chern number gives a straightforward means of checking whether a given system has edge states and, therefore, if it will be robust to various forms of

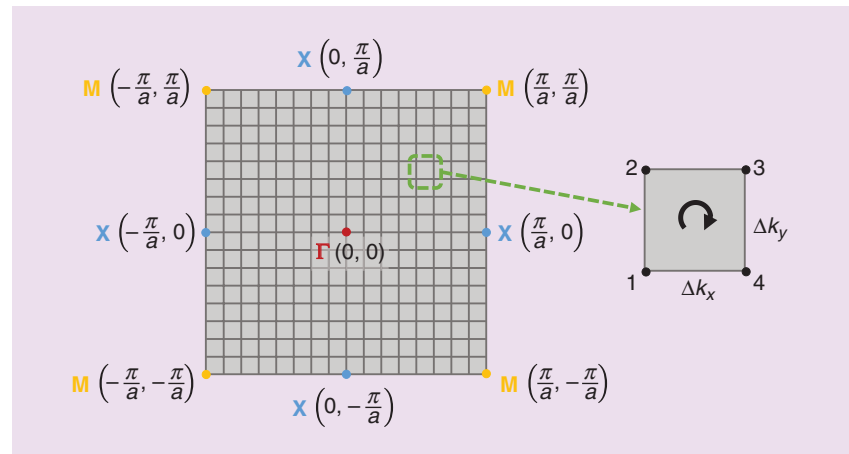


FIGURE 5. The discretization of a square 2D BZ in the increment of Δk_x in x direction and Δk_y in the y direction. A hexagonal BZ can be discretized into a parallelogram grid in a similar manner.

disorder. We have provided a collection of general-purpose MATLAB functions that perform the various steps, available via a public repository [26]. It is worth noting that these numerical methods are not the only option to determine the nontriviality of a system, with another powerful technique being the Green's function approach (which also simplifies the analysis of degenerated bands)

SIDE NOTE 5

Computing the Berry curvature and topological invariant for degenerate modes is slightly different than for the other types since they involve a combination of modes. To account for multiple modes, it is necessary to change the representation of the Berry connection to a matrix where each element is the Berry connection between a pair of modes [23]. For the common case of a single degenerate pair, the matrix takes the form of

$$S_{kk'} = \begin{pmatrix} \langle E_k^1 | E_{k'}^1 \rangle & \langle E_k^1 | E_{k'}^2 \rangle \\ \langle E_k^2 | E_{k'}^1 \rangle & \langle E_k^2 | E_{k'}^2 \rangle \end{pmatrix}, \quad (S3)$$

where the superscripts correspond to the band index. With this formulation, the Berry curvature for a given cell is given by

$$\Omega(k_x, k_y) \Delta k_x \Delta k_y = -i(\ln(\det(S_{k_1 k_2} S_{k_2 k_3} S_{k_3 k_4} S_{k_4 k_1}))). \quad (S4)$$

Equation (S4) can be generalized to as many degenerate bands as necessary [23], [25].

SIDE NOTE 6

The topological phase transition is the procedure where a system changes its topological invariant. Systems with different topological invariants cannot change into each other without a phase transition. In periodic systems, this occurs when a bandgap closes, marked by a change in the Chern number. In PhCs, a topological transition is usually induced by changes in the symmetry or geometry of the PhC unit cell.

[27]. In the proceeding sections, we show example calculations of each PTI type (Chern, valley, and spin) using this code, with the eigenmode data simulated via the Ansys high-frequency structure simulator.

The Chern number describes the topology of a band and characterizes the most fascinating and technologically relevant phenomena: topologically “protected” edge states. These edge states appear at the interface between two structures with unequal Chern numbers.

Unlike traditional photonic waveguides, with a trivial edge state between two ordinary insulators (with a Chern number of zero), the nontrivial edge waveguide formed by these two topologically inequivalent structures (at least one structure is of a nonzero Chern number) would be immune to defects and backscattering. This is because, when two domains with different topological invariants are connected directly to form an interface, a topological phase transition must happen at the interface [2] (see “Side Note 6”).

Essentially, the differing topologies mean that the respective bands in each bandgap material cannot be continuously transformed into one another. Transforming one into the other requires the frequency gap to close at the interface and then reopen on the other side. This phase transition gives rise to the gapless edge states at the interface. To accommodate the jump in the Chern number's integer value, e.g., from 1 to 0, 1 to -1, and so on, the number of gapless edge modes turns out to be the difference of the Chern numbers across the interface [28]. This is known as the *bulk-edge correspondence* [2].

SIDE NOTE 7

The most useful symmetries for EM systems are as follows:

- *TRS*: $t \rightarrow -t$, broken by gyrotropic materials with applied E-/H-fields
- *spatial-inversion symmetry*: $\mathbf{r} \rightarrow -\mathbf{r}$, broken by altering the geometry of the material (e.g., removing a slice from a cylinder or changing circles to triangles).

These gapless modes are tied to the bulk Chern numbers, so they are robust and must always exist, regardless of the specific shape of the boundary (unlike conventional waveguides) [2]. It is worth stressing that these modes are distinct from those found in standard PhC waveguides (which can also possess high robustness [29]), with the primary difference being that their immunity to certain forms of scattering is a global property of the bulk rather than any specific arrangement of PhC cells.

CHERN PTIs

In general, PhCs and other periodic structures have a zero Chern number [2]. To engineer one, we need to focus on two key steps: 1) finding a degenerate point between the bands and 2) breaking a symmetry that opens a bandgap near that point (see “Side Note 7”). This section details how the simplest type of PTI, the Chern PTI, is constructed and demonstrates the exciting features it has for practical designs. This type of structure is a direct emulation of the QHE discussed previously [30].

The first step, finding degeneracies, relates to the abrupt nature of the Chern number: a material can change its Chern number (a topological phase transition) only when two or more photonic bands are degenerate at a point. This is part of the reason for the robustness of edge modes, as any small change to the structure that keeps the bandgap open in the bulk does not affect the mode. Finding a degeneracy in PhCs is common, but the second step, opening a bandgap via a broken symmetry, places some restrictions on the degeneracies that are useful for making a PTI [2].

The simplest type of degenerate point for PTIs is a linear crossing of two bands, often called a *Dirac cone* in the literature [4]. Such a crossing can be made via a PhC in a honeycomb lattice, where the degenerate point will always occur at the $K(K')$ high-symmetry point in the BZ [1]. To obtain a nontrivial PhC, it is, however, not necessary to form a linear-type degeneracy, as any other type (e.g., quadratic [31] or accidental [32]) will also work.

To see how this works for a real device, we use the example of

Wang et al. [33], which was later developed into the first experimental demonstration of a Chern PTI [34]. First, to create the initial degenerate point, we select a square lattice of circular rods [chosen to be made of yttrium–iron–garnet, (YIG), for reasons soon explained] and tune the geometry to find a quadratic crossing of the second and third bands at the M point, shown in Figure 6(a). Note that there is also a degeneracy at the Γ point for the third and fourth bands, but we focus on the quadratic M point here.

Now that we have our degeneracy, we must break a symmetry that opens a complete bandgap near it. The chief symmetries present in the system are the TRS (where running time backward does not affect the response) and SIS (where flipping the coordinate axes maintains the shape and orientation of the unit cell).

Breaking either will induce a bandgap, but only breaking the TRS will cause a nonzero accumulation of the Berry phase over the whole BZ and, so, will result in the desired edge modes [24]. Following Wang et al.’s approach, the TRS can be broken by applying a static magnetic field perpendicular to the 2D plane. Doing so induces an anisotropy to the magnetic permeability of the YIG with the form

$$\tilde{\mu} = \begin{bmatrix} \mu & i\kappa & 0 \\ -i\kappa & \mu & 0 \\ 0 & 0 & \mu_0 \end{bmatrix}. \quad (21)$$

Here, κ represents the effect of the z -directed dc magnetic field and is zero when the field is turned off. For a 1,600-G magnetic field [33], the values at 4.28 GHz are $\kappa = 12.4\mu_0$ and $\mu = 14\mu_0$, with μ_0 being the vacuum permeability in meter–kilogram–seconds. Breaking the TRS by turning on the magnetic field opens a bandgap near the degenerate point for the second and third bands at the M point, as shown in Figure 6(b).

To confirm that the opened bandgap is indeed topologically nontrivial, we can observe the behavior of the Berry curvature for the various bands, shown in Figure 7(a) and (b). We can see that the second mode has a very large contribution to the Berry curvature right at the M point and, likewise, for the X point of the third mode. Integrating over each separately, we find the Chern number of the lowest band to be zero, while the next three are -1 , 2 , and 1 , indicating the existence of edge modes within the upper bandgaps.

An important thing to note is that, while the Chern number C_n is associated with each band n of the bulk, edge modes are associated with the bandgaps between them. To differentiate this, we often speak of the “gap Chern number” $C_{\text{gap}} = \sum_{n < n_g} C_n$, which is just the sum of the Chern numbers of all bands below a given bandgap with upper band n_g [16]. Hence, to observe edge modes, we need to operate within a bandgap between two materials with

different gap Chern numbers, with the net number of modes being their difference: $N_{\text{modes}} = C_{\Delta\text{gap}} = |C_{\text{gap},1} - C_{\text{gap},2}|$. For this example, that implies the lowest bandgap will have no edge modes (or, more precisely, the net number of rightward modes equals the net number of leftward modes [35]), while the second and third bandgaps will.

The magnetized YIG model displays all of the telltale signs of a Chern PTI, and, as such, we can construct a wide range of devices that exploit its nonreciprocal and highly robust nature. One such demonstration is an isolating transmission line with two 90° bends, shown in Figure 7(c) and (d) (compare with Figure 1). Similar to ferrite-based magnetic isolators, the device is nonreciprocal for any EM mode inside the nontrivial bandgaps, but there are a few important and highly attractive features:

- Unlike a traditional isolator, EM energy is not simply routed to a lumped element load and dissipated locally as heat [34]. Instead, the influence of the Berry phase results in an edge mode only for a single direction of propagation, with no allowed modes in the opposite direction. Hence, any energy sent the opposite way will either be reflected or decay exponentially into the bulk in the same manner as a trivial PhC [Figure 7(d)].
- The directionality of the mode is determined by the direction of the

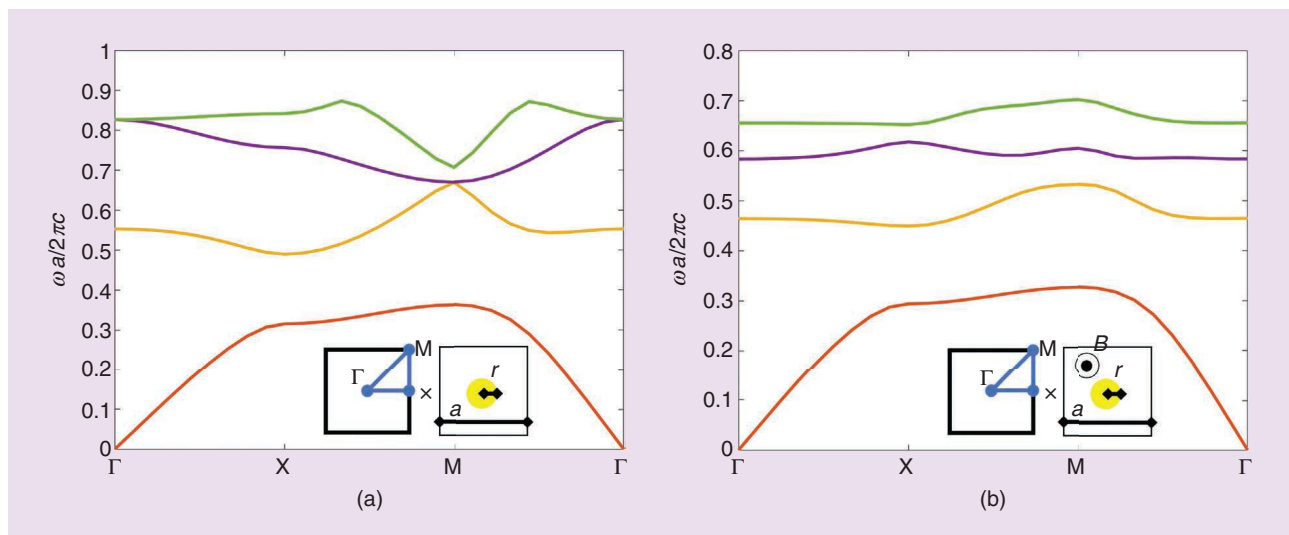


FIGURE 6. A band diagram for the square lattice of (a) unmagnetized and (b) magnetized YIG rods in air. The inset in (a) shows the BZ path, and the inset in (b) represents a unit cell with $r = 0.11a$.

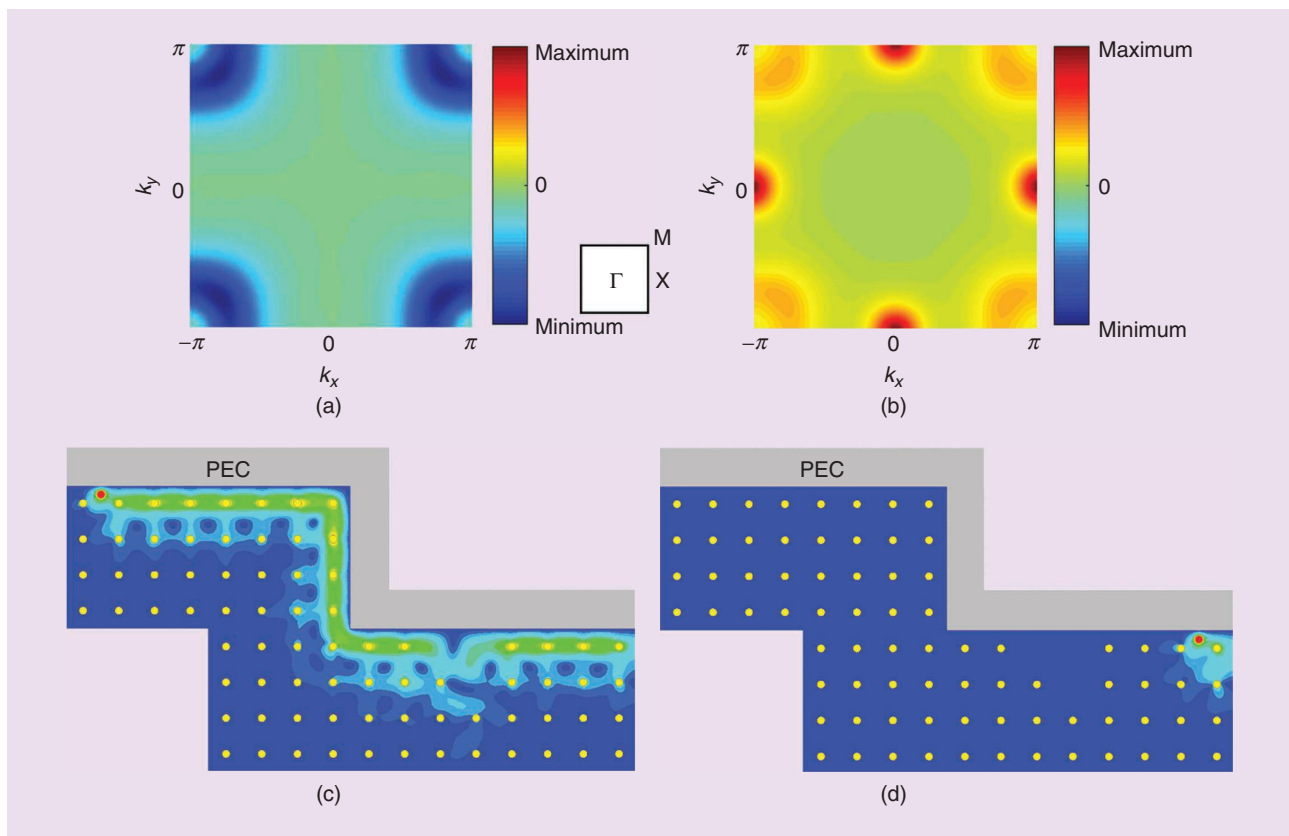


FIGURE 7. Proving nontrivial transport for a magnetically biased Chern PTI. (a) The Berry curvature for the second band, showing large dips near the M point. The middle inset shows the BZ diagram. (b) The Berry curvature for the third band, with sharp peaks at the X point and smaller peaks at the M point. (c) An example of robust transport, with two 90° bends and a defect along the path. Note the lack of backscatter. (d) Exciting the same structure from the other end shows the isolator-like behavior, with no mode for propagation in the opposite direction. PEC: perfect electric conductor.

SIDE NOTE 8

Although the example of a Chern PTI studied here concerns periodic structures with discrete translational symmetry, it has been recently shown that Chern numbers can also be defined for continuous media, such as a homogenous magnetized plasma [51]. In addition, other platforms, including arrays of coupled waveguides, can be used to emulate the effect at optical frequencies [38].

Reference

[51] M. G. Silveirinha, "Chern invariants for continuous media," *Phys. Rev. B*, vol. 92, no. 12, p. 125153, Sept. 2015. doi: 10.1103/PhysRevB.92.125153.

bias magnetic field, so flipping its direction will also flip the allowed propagation direction.

- With the lack of backward modes, a source of backscatter, like the

shown 90° bends, will force the energy around corners with negligible losses. This will occur so long as the strength of the scatterer is not greater than the size of the nontrivial bandgap, provided the scatterer is nonmagnetic [2]. Likewise, any small defect, like the three missing rods, will not lead to scattering.

- Being essentially a distributed device, the level of isolation and insertion loss can be tuned by varying the length and shape of the structure.

This example is for a 2D system, which can be experimentally emulated via a parallel-plate waveguide structure, with the separation between the plates being very thin, ensuring only TM modes can propagate. This platform makes it easy to analyze but is less straightforward to integrate into normal EM and photonic systems. However, there are numerous studies and ongoing work to create Chern PTIs for more practical

settings [36]. A major breakthrough for this line of research was the development of the valley and spin PTIs (detailed in the following sections), which remove the requirement of the external magnetic field (see "Side Note 8").

VALLEY PTIs

Although the Chern PTI has many advantages, the requirement for magneto-optical materials and external magnetic fields places limits on the practical applications. The question then arises: can we construct a PTI with similar features of robustness to disorder or sharp turns while still being reciprocal? The answer turns out to be yes, with some limitations. There is another type of PTI made of passive materials that exploits an inherent degree of freedom of hexagonal lattices that can be used to mimic similar phenomena for robust edge state propagation, although the level of robustness depends on the types of disorder considered.

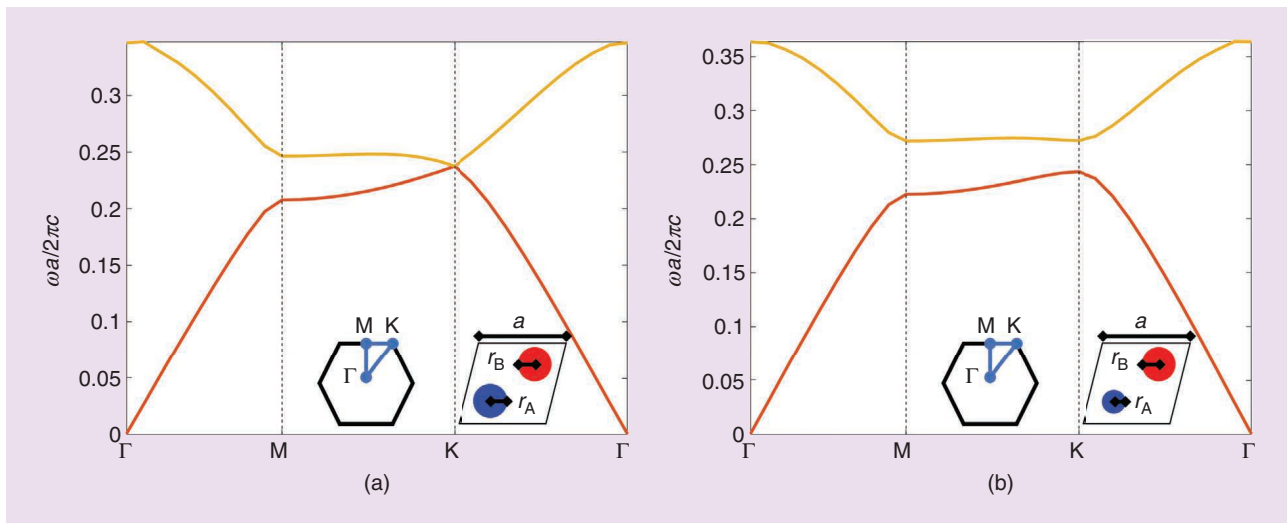


FIGURE 8. The band diagram for the (a) symmetrical (trivial) and (b) asymmetrical (nontrivial) valley structure, with silicon ($\epsilon_r = 11.9$) rods in air. The inset in (a) shows the BZ path, and the inset in (b) represents the unit cell, with (a) $r_A = r_B = 0.25a$ and (b) $r_A = 0.19a$, $r_B = 0.25a$.

Specifically, in a hexagonal/graphene-like lattice, the angular rotation of the E-fields at the high-symmetry point K or K' generates an intrinsic magnetic moment, which is called the *valley degree of freedom* [19]. The term *valley* is used owing to the shape of the dispersion near the K (K') point, which, in a triangular lattice, is a deep dip, or a sharp peak, both of which are referred to as valleys. Just as the Chern PTI emulates the QHE, the valley PTI is a model for the “quantum valley Hall effect,” studied in graphene-like materials.

To design a valley PTI, we can start from a graphene-like PhC, which possesses the “Dirac”-like degenerate point at the K (K') point. Such a lattice can be constructed by a unit cell containing two rods of equal radius (A and B sites), shown in the inset to Figure 8(a). Like when constructing a Chern PTI, a symmetry must be broken to lift the degeneracy. In a valley PTI, a controllable bandgap can be achieved by differentiating the A and B rods in the unit cell, thus breaking the inversion symmetry. As we show through examples, a graphene-like PhC that lacks inversion symmetry exhibits opposite Berry curvatures at the K and K' points [23]. In principle, this allows us to selectively couple to either the K or K' valleys, which would result in a unidirectional topologically protected edge mode that is locked to the direction of Γ to K or Γ to K' .

Here, we look at an example of a dielectric valley PTI from [39]. Each unit cell consists of two silicon rods, A and B, with corresponding radii r_A and r_B . When r_A and r_B are identical (here, $r_A = r_B = 0.25a$, with lattice constant a), the structure becomes a type of photonic graphene, and there is a Dirac degeneracy at the K (K') point as shown in Figure 8(a).

We then break the inversion symmetry by shrinking the A rod slightly ($r_A = 0.19a$). This lifts the degeneracy and opens a complete bandgap around

it, as shown in Figure 8(b). Note that we can tune this bandgap by tuning the dimensions of A and/or B. The more different A and B are, the larger the bandgap.

As shown in Figure 9, the in-plane E-field distribution of the first and second bands at the K valley are accompanied by an energy flux (i.e., time-averaged Poynting vectors) rotating in either a clockwise or counterclockwise manner. In accordance with the TRS, we also find that the field profile at the K' valley exhibits the reversed direction

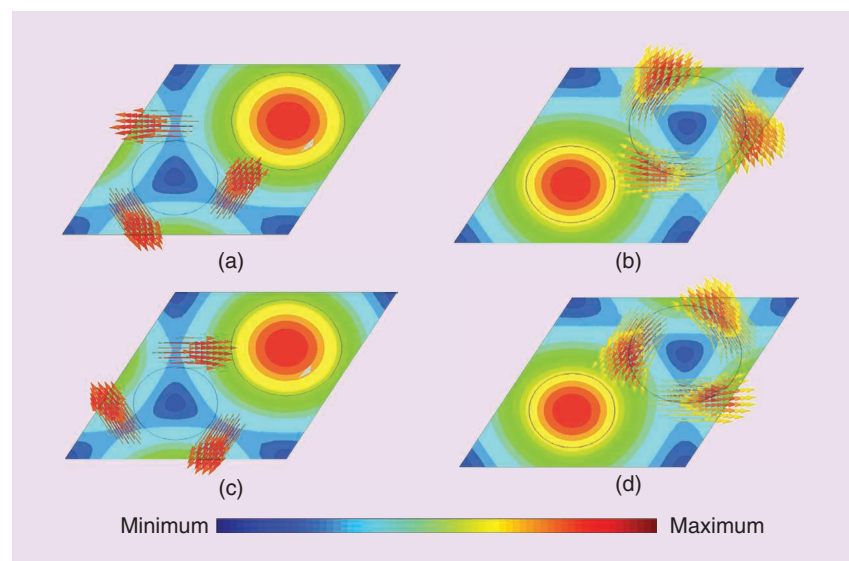


FIGURE 9. The difference in energy flux of the K and K' modes for the upper and lower bands. The color denotes the magnitude of the E-field, while the arrows are the real part of the Poynting vector: the (a) lower and (b) upper bands at K as well as the (c) lower and (d) upper bands at K' .

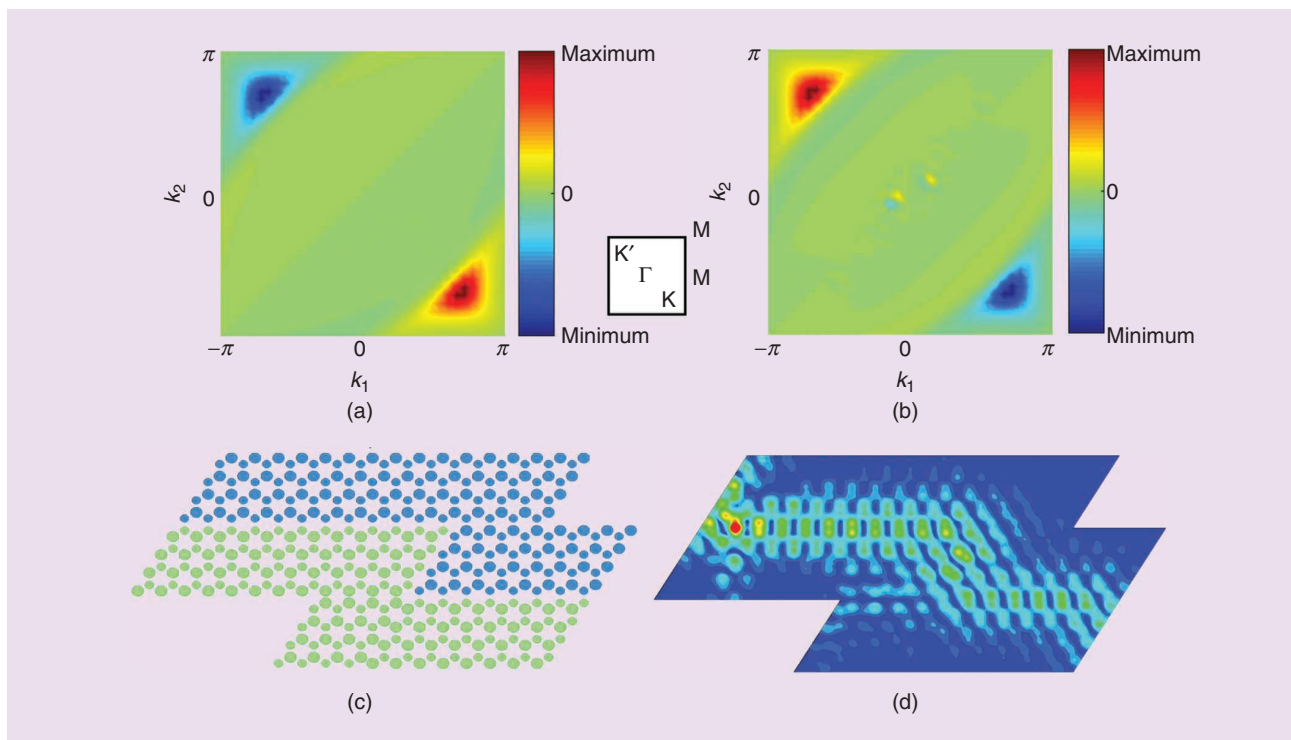


FIGURE 10. Proving the nontrivial transport of a valley PTI of two-site silicon rods. (a) The Berry curvature for the lower band. The middle inset illustrates the BZ diagram. (b) The Berry curvature of the upper band, showing flipped peaks and nulls from the lower-band case. (c) The interface structure with two 120° bends. The two regions are simply rotated versions of each other. (d) The magnitude of the E-field of the structure.

of energy flux. The flux vortex's center corresponds to a singular point of the phase (here, the out-of-plane E-field E_z), carrying an orbital angular momentum (OAM) with its sign depending on the vortex direction [39].

This vortex can be considered as an “artificial magnetic field”-like effect that replaces the role of the real magnetic field of the Chern PTI. Meanwhile, inverting the orientation of the unit cells in the plane (i.e., swapping the A and B lattice sites) results in identical band structures but opposite signs of the OAM at the K and K' valleys. Importantly, the frequency order of the OAM states at each valley is also inverted, which indicates a topological phase transition.

To further validate the nontrivial topological character of the bands, we can numerically calculate the Berry curvature, as shown in Figure 10(a) and (b). The spike at the K point results in a Berry phase of π , while there is a $-\pi$ Berry phase accumulation at K' . Integrating over half of the BZ [or near K (K')], we get the valley Chern number of $+(1/2)$ for K and $-(1/2)$ for K' . If the A and

B sites are exchanged, we get the valley Chern number of $-(1/2)$ for K and $+(1/2)$ for K' (see “Side Note 9”).

Furthermore, we can see that the signs of both flip from the lower band to the higher band. This indicates that valley-polarized topological edge states exist within the bandgap at an interface between structures with opposite unit cell orientations (between A–B and B–A). The interface will, therefore, have A sites adjacent to A sites or B sites adjacent to B sites. The number of edge modes at each valley, in accordance with

the bulk-edge correspondence, is determined by the difference of C_v above and below the bandgap: $C_{v,2}^K - C_{v,1}^K = 1$, $C_{v,2}^{K'} - C_{v,1}^{K'} = -1$, where each value corresponds to a single valley (K or K'). The differing signs here could be interpreted as the sign of the group velocity of the forward- and backward-propagating modes at the two valleys [19].

We can again build, essentially, the same bent waveguiding model as the Chern PTI to demonstrate the robustness of the valley structure, shown in Figure 10(c) and (d). The valley PTIs also have their own features (see “Side Note 10”):

- Unlike the Chern PTIs (and spin PTIs), where topological edge modes can be formed at the interface between nontrivial and trivial lattices, the valley edge modes exist only at the interface between two valley PTIs with opposite valley Chern numbers ($(1/2)$ and $-(1/2)$). Therefore, when constructing a valley waveguide, there must always be a pair of complementary valley PhCs.
- Since the valley edge modes are coupled to K or K' valleys, these

SIDE NOTE 9

How can the “valley Chern number” be $\pm(1/2)$ when the Chern number is always an integer? The value is only guaranteed to be an integer when the integrated curvature is closed, while, here, we consider only half the BZ, which is, therefore, open. Valley PTIs gain their characteristics by the opposite behavior at K and K' , even though the “true” Chern number is zero.

edge modes are the most robust in the directions where the valleys are clearly defined (i.e., the Γ -to- K or Γ -to- K' directions), indicating that they will preserve their unidirectionality only when sharp turns are 120° . In contrast to Chern PTIs, defects that scatter valleys into each other (breaking the C_{3v} symmetry, for example) will weaken the edge mode and give lower robustness [40].

- Valley states can couple to spin-type modes in certain PTIs [41]. These spin–valley coupled edge states can be used to form “valley splitters” that are not restricted by the orientation of the unit cell [41].
- Unlike many spin PTI designs, it is simple to construct planar or nearly planar valley PTIs, making them an attractive choice for integration with normal silicon [42] or metal-on-insulator designs.

SPIN PTIs

The last major PTI type, the spin PTI, is, in a practical sense, similar to the valley type, being reciprocal while still possessing highly robust features. A full example of a recently demonstrated planar metallic PTI [44], which has a number of attractive features for integration with traditional microwave systems [45], is provided in the additional online materials. Spin PTIs are also readily adaptable to dielectric platforms suitable for optical bands [46].

CONCLUSIONS AND FUTURE OUTLOOK

In this tutorial, we have given an overview of the concepts, mathematics, and implementations of PTIs. The central idea that relates the topics together is the geometric phase, which lies at the heart of both theory and physical realization. This concept is readily applied to a 2D PhC, which is a simple platform to engineer topological modes. Computations of the Berry curvature, Chern number, and other topological invariants for a given design illuminate how the geometric phase influences the system and can be readily calculated with numerical tools to aid in design.

The three most common formulations of PTIs, the Chern, valley, and spin PTIs, all represent different strategies to

SIDE NOTE 10

It is also possible to build a purely metallic valley PTI. For example, a valley PTI can be constructed by a patch-type flat metasurface to engineer transverse electric modes (or apertures for transverse magnetic modes) [52]. Simply changing the shape of the patch from a hexagon into a triangle reduces the cell from a 60° to 120° rotation symmetry. As a result, the degenerate bands split at the two inequivalent but time-reversed valleys (K and K'), leading to a bandgap in the BZ. Edge modes will form between sheets of upward- and downward-pointed triangles.

Reference

[52] D. J. Bisharat and D. F. Sievenpiper, “Topological metasurfaces for symmetry-protected electromagnetic line waves,” in *Proc. SPIE Nanosci. Eng.*, San Diego, CA, Aug. 12, 2019. doi: 10.1117/12.2529727.

achieve the effects of topologically protected modes, lending considerable flexibility to their usage. In all cases, such devices possess remarkable robustness to a wide class of disorder, which could enable much greater fabrication tolerances for applications like extremely robust integrated optical waveguides [38]. Likewise, their immunity to backscattering off of sharp bends has the potential to shrink device footprints by eliminating the gradual bends or careful engineering needed at the edges to overcome losses or higher-order mode mixing when a turn is required in a waveguide [2], [36].

For the case of the Chern PTI devices, there is a large effort to deploy topologically protected lasers [47], with many recent studies realizing arbitrarily shaped optical cavities immune to disorder [48]. Further uses can be seen in isolators [34] and circulators [37]. In the magnetic field-free valley and spin implementations, there is potential to use such devices in place of traditional transmission lines or waveguides, with the added benefits of sharp bend immunity and robustness to disorder [40], [44].

For microwave devices, many of these are functionally similar to traditional metallic structures, and, as such, could

be integrated into standard systems with relative ease [40]. At optical frequencies, topologically protected designs could enable features like spin-selective filtering [43] and unidirectional polarization control [19] beyond general robustness.

ONLINE SUPPLEMENTARY MATERIAL

This article has supplementary downloadable material available at <https://doi.org/10.1109/map.2021.3069276>, provided by the authors.



AUTHOR INFORMATION

Dia'aaldin J. Bisharat (dbisharat@ucsd.edu) is a postdoctoral researcher at the City University of New York Graduate Center, New York, New York, 10016, USA. Previously, he was with the University of California, San Diego, La Jolla. His research interests include novel approaches for guiding electromagnetic waves. He is a Member of IEEE.

Robert J. Davis (rjdavis@ucsd.edu) is a Ph.D. student at the University of California, San Diego, La Jolla, California, 92093, USA. His research interests include applying new concepts from condensed-matter physics to electromagnetic problems. He is a Student Member of IEEE.

Yun Zhou (yuz421@eng.ucsd.edu) is a Ph.D. student at the University of California, San Diego, La Jolla, California, 92093, USA. Her research interests include phononic topological insulators. She is a Fellow of IEEE.

Prabhakar R. Bandaru (pbandaru@ucsd.edu) is a professor at the University of California, San Diego, La Jolla, California, 92093, USA. His research interests include electrochemical energy storage, control of thermal energy, and fluid flow at the nanoscale. He is a Fellow of IEEE.

Daniel F. Sievenpiper (dsievenpiper@eng.ucsd.edu) is a professor at the University of California, San Diego, La Jolla, California, 92093, USA. His research interests include

electromagnetics, periodic structures, and wave phenomena. He is a Fellow of IEEE.

REFERENCES

- [1] J. Joannopoulos, S. G. Johnson, J. N. Winn, and D. M. Robert, *Photonic Crystals: Molding the Flow of Light*. Princeton, NJ: Princeton Univ. Press, 2008.
- [2] T. Ozawa et al., "Topological photonics," *Rev. Mod. Phys.*, vol. 91, no. 1, p. 015006, Mar. 2019. doi: 10.1103/RevModPhys.91.015006.
- [3] D. J. Thouless, M. Kohmoto, M. P. Nightingale, and M. den Nijs, "Quantized hall conductance in a two-dimensional periodic potential," *Phys. Rev. Lett.*, vol. 49, no. 6, pp. 405–408, Aug. 1982. doi: 10.1103/PhysRevLett.49.405.
- [4] F. D. M. Haldane, "Model for a quantum hall effect without landau levels: Condensed-matter realization of the 'parity anomaly'," *Phys. Rev. Lett.*, vol. 61, no. 18, pp. 2015–2018, Oct. 1988. doi: 10.1103/PhysRevLett.61.2015.
- [5] M. Z. Hasan and C. L. Kane, "Colloquium: Topological insulators," *Rev. Mod. Phys.*, vol. 82, no. 4, pp. 3045–3067, Nov. 2010. doi: 10.1103/RevModPhys.82.3045.
- [6] B. Simon, "Holonomy, the quantum adiabatic theorem, and Berry's phase," *Phys. Rev. Lett.*, vol. 51, no. 24, pp. 2167–2170, Dec. 1983. doi: 10.1103/PhysRevLett.51.2167.
- [7] M. Nakahara, *Geometry, Topology and Physics*, 2nd ed. Bristol (PA): CRC Press, 2003.
- [8] A. Bansil, H. Lin, and T. Das, "Colloquium: Topological band theory," *Rev. Mod. Phys.*, vol. 88, no. 2, p. 021004, June 2016. doi: 10.1103/RevModPhys.88.021004.
- [9] X.-L. Qi and S.-C. Zhang, "Topological insulators and superconductors," *Rev. Mod. Phys.*, vol. 83, no. 4, pp. 1057–1110, Oct. 2011. doi: 10.1103/RevModPhys.83.1057.
- [10] H.-X. Wang, G.-Y. Guo, and J.-H. Jiang, "Band topology in classical waves: Wilson-loop approach to topological numbers and fragile topology," *New J. Phys.*, vol. 21, no. 9, p. 093029, Sept. 2019. doi: 10.1088/1367-2630/ab371.
- [11] F. Wilczek and A. Shapere, *Geometric Phases in Physics*, vol. 5. Singapore: World Scientific, 1989.
- [12] S. Pancharatnam, "Generalized theory of interference, and its applications," *Proc. Indian Acad. Sci.*, vol. 44, no. 5, pp. 247–262, Nov. 1956. doi: 10.1007/BF03046050.
- [13] M. V. Berry, "Quantal phase factors accompanying adiabatic changes," *Proc. Math. Phys. Eng. Sci.*, vol. 392, no. 1802, pp. 45–57, Mar. 1984. doi: 10.1098/rspa.1984.0023.
- [14] J. von Bergmann and H. von Bergmann, "Foucault pendulum through basic geometry," *Am. J. Phys.*, vol. 75, no. 10, pp. 888–892, Sept. 2007. doi: 10.1119/1.2757623.
- [15] R. Y. Chiao and Y.-S. Wu, "Manifestations of Berry's topological phase for the photon," *Phys. Rev. Lett.*, vol. 57, no. 8, pp. 933–936, Aug. 1986. doi: 10.1103/PhysRevLett.57.933.
- [16] S. A. Hassani Gangaraj, M. G. Silveirinha, and G. W. Hanson, "Berry phase, berry connection, and Chern number for a continuum bianisotropic material from a classical electromagnetics perspective," vol. 2, pp. 3–17, 2017. doi: 10.1109/JMMCT.2017.2654962.
- [17] E. Cohen, H. Larocque, F. Bouchard, F. Nejadattari, Y. Gefen, and E. Karimi, "Geometric phase from Aharonov–Bohm to Pancharatnam–Berry and beyond," *Nat. Rev. Phys.*, vol. 1, no. 7, pp. 437–449, July 2019. doi: 10.1038/s42254-019-0071-1.
- [18] X. Cheng, C. Jouvaud, X. Ni, S. H. Mousavi, A. Z. Genack, and A. B. Khanikaev, "Robust reconfigurable electromagnetic pathways within a photonic topological insulator," *Nat. Mater.*, vol. 15, no. 5, pp. 542–548, May 2016. doi: 10.1038/nmat4573.
- [19] T. Ma and G. Shvets, "All-Si valley-Hall photonic topological insulator," *New J. Phys.*, vol. 18, no. 2, p. 025012, Feb. 2016. doi: 10.1088/1367-2630/18/2/025012.
- [20] A. B. Khanikaev, S. Hossein Mousavi, W.-K. Tse, M. Kargarian, A. H. MacDonald, and G. Shvets, "Photonic topological insulators," *Nat. Mater.*, vol. 12, no. 3, pp. 233–239, Mar. 2013. doi: 10.1038/nmat3520.
- [21] T. Ma, A. B. Khanikaev, S. H. Mousavi, and G. Shvets, "Guiding electromagnetic waves around sharp corners: Topologically protected photonic transport in metawaveguides," *Phys. Rev. Lett.*, vol. 114, no. 12, p. 127401, Mar. 2015. doi: 10.1103/PhysRevLett.114.127401.
- [22] L. Fu and C. L. Kane, "Topological insulators with inversion symmetry," *Phys. Rev. B*, vol. 76, no. 4, p. 045302, July 2007. doi: 10.1103/PhysRevB.76.045302.
- [23] M. B. de Paz et al., "Tutorial: Computing topological invariants in 2D photonic crystals," *Adv. Quantum Technol.*, vol. 3, no. 2, p. 1900117, 2020. doi: 10.1002/qute.201900117.
- [24] C. Wang, H. Zhang, H. Yuan, J. Zhong, and C. Lu, "Universal numerical calculation method for the Berry curvature and Chern numbers of typical topological photonic crystals," *Front. Optoelectron.*, vol. 13, pp. 73–88, Jan. 2020. doi: 10.1007/s12200-019-0963-9.
- [25] T. Fukui, Y. Hatsugai, and H. Suzuki, "Chern numbers in discretized Brillouin zone: Efficient method of computing (spin) Hall conductances," *J. Phys. Soc. Jpn.*, vol. 74, no. 6, pp. 1674–1677, June 2005. doi: 10.1143/PSJ.74.1674.
- [26] "UCSD applied electromagnetics lab." Github. <https://github.com/Applied-Electromagnetics-Lab> (accessed Apr. 8, 2021.)
- [27] F. R. Prudêncio and M. G. Silveirinha, "First principles calculation of topological invariants of non-Hermitian photonic crystals," *Commun. Phys.*, vol. 3, Dec. 2020, Art. no. 221. doi: 10.1038/s42005-020-00482-3.
- [28] Y. Hatsugai, "Chern number and edge states in the integer quantum Hall effect," *Phys. Rev. Lett.*, vol. 71, no. 22, pp. 3697–3700, Nov. 1993. doi: 10.1103/PhysRevLett.71.3697.
- [29] A. Mekis, J. C. Chen, I. Kurland, S. Fan, P. R. Villeneuve, and J. D. Joannopoulos, "High transmission through sharp bends in photonic crystal waveguides," *Phys. Rev. Lett.*, vol. 77, no. 18, pp. 3787–3790, Oct. 1996. doi: 10.1103/PhysRevLett.77.3787.
- [30] F. D. M. Haldane and S. Raghu, "Possible realization of directional optical waveguides in photonic crystals with broken time-reversal symmetry," *Phys. Rev. Lett.*, vol. 100, p. 013904, Jan. 2008. doi: 10.1103/PhysRevLett.100.013904.
- [31] Y. D. Chong, X.-G. Wen, and M. Soljačić, "Effective theory of quadratic degeneracies," *Phys. Rev. B*, vol. 77, no. 23, p. 235125, June 2008. doi: 10.1103/PhysRevB.77.235125.
- [32] L. Xu, H.-X. Wang, Y.-D. Xu, H.-Y. Chen, and J.-H. Jiang, "Accidental degeneracy in photonic bands and topological phase transitions in two-dimensional core-shell dielectric photonic crystals," *Opt. Express*, vol. 24, no. 16, pp. 18,059–18,071, Aug. 2016. doi: 10.1364/OE.24.018059.
- [33] Z. Wang, Y. D. Chong, J. D. Joannopoulos, and M. Soljačić, "Reflection-free one-way edge modes in a gyromagnetic photonic crystal," *Phys. Rev. Lett.*, vol. 100, p. 013905, Jan. 2008. doi: 10.1103/PhysRevLett.100.013905.
- [34] Z. Wang, Y. Chong, J. D. Joannopoulos, and M. Soljačić, "Observation of unidirectional backscattering-immune topological electromagnetic states," *Nature*, vol. 461, no. 7265, pp. 772–775, Oct. 2009. doi: 10.1038/nature08293.
- [35] M. G. Silveirinha, "Proof of the bulk-edge correspondence through a link between topological photonics and fluctuation-electrodynamics," *Phys. Rev. X*, vol. 9, p. 011037, Feb. 2019. doi: 10.1103/PhysRevX.9.011037.
- [36] S. Ma and S. M. Anlage, "Microwave applications of photonic topological insulators," *Appl. Phys. Lett.*, vol. 116, no. 25, p. 250,502, June 2020. doi: 10.1063/5.0008046.
- [37] S. Ma, B. Xiao, Y. Yu, K. Lai, G. Shvets, and S. M. Anlage, "Topologically protected photonic modes in composite quantum Hall/quantum spin Hall waveguides," *Phys. Rev. B*, vol. 100, no. 8, p. 085118, Aug. 2019. doi: 10.1103/PhysRevB.100.085118.
- [38] M. Hafezi, E. A. Demler, M. D. Lukin, and J. M. Taylor, "Robust optical delay lines with topological protection," *Nat. Phys.*, vol. 7, no. 11, pp. 907–912, Nov. 2011. doi: 10.1038/nphys2063.
- [39] X.-D. Chen, F.-L. Zhao, M. Chen, and J.-W. Dong, "Valley-contrasting physics in all-dielectric photonic crystals: Orbital angular momentum and topological propagation," *Phys. Rev. B*, vol. 96, no. 2, p. 020202, July 2017. doi: 10.1103/PhysRevB.96.020202.
- [40] B. Orazbayev and R. Fleury, "Quantitative robustness analysis of topological edge modes in C6 and valley-Hall metamaterial waveguides," *Nanophotonics*, vol. 8, no. 8, pp. 1433–1441, 2019. doi: 10.1515/nanoph-2019-0137.
- [41] Y. Kang, X. Ni, X. Cheng, A. B. Khanikaev, and A. Z. Genack, "Pseudo-spin–valley coupled edge states in a photonic topological insulator," *Nat. Commun.*, vol. 9, Aug. 2018, Art. no. 3029. doi: 10.1038/s41467-018-05408-w.
- [42] X.-T. He et al., "A silicon-on-insulator slab for topological valley transport," *Nat. Commun.*, vol. 10, p. 872, Feb. 2019. doi: 10.1038/s41467-019-08881-z.
- [43] M. P. Makwana and G. Chaplain, "Tunable three-way topological energy-splitter," *Sci. Rep.*, vol. 9, Dec. 2019, Art. no. 18939. doi: 10.1038/s41598-019-55485-0.
- [44] D. J. Bisharat and D. F. Sievenpiper, "Electromagnetic-dual metasurfaces for topological states along a 1D interface," *Laser Photonics Rev.*, vol. 13, no. 10, p. 1900126, 2019. doi: 10.1002/lpor.201900126.
- [45] R. J. Davis, D. J. Bisharat, D. F. Sievenpiper, "Efficient transition from a planar transmission to a topological line wave," in *Proc. IEEE Antennas Propag. Symp. North Amer. Radio Sci. Meeting*, Montreal, Canada, July 5–10, 2020, pp. 757–758. doi: 10.1109/IEEECONF35879.2020.9329833.
- [46] A. Slobozhanyuk et al., "Near-field imaging of spin-locked edge states in all-dielectric topological metasurfaces," *Appl. Phys. Lett.*, vol. 114, no. 3, p. 031103, Jan. 2019. doi: 10.1063/1.5055601.
- [47] G. Harari et al., "Topological insulator laser: Theory," *Science*, vol. 359, no. 6381, p. eaar4003, Mar. 2018. doi: 10.1126/science.aar4003.
- [48] B. Bahari, A. Ndao, F. Vallini, A. E. Amili, Y. Faiman, and B. Kanté, "Nonreciprocal lasing in topological cavities of arbitrary geometries," *Science*, vol. 358, no. 6363, pp. 636–640, Nov. 2017. doi: 10.1126/science.aao4551.

